BiOBr/MoS2 catalyst as heterogenous peroxymonosulfate activator toward organic pollutant removal: Energy band alignment and mechanism insight

ZHANG, Bofan, ZHANG, Mutian, ZHANG, Liang, BINGHAM, Paul <http://orcid.org/0000-0001-6017-0798>, TANAKA, Manabu, LI, Wen and KUBUKI, Shiro

Published version

ZHANG, Bofan, ZHANG, Mutian, ZHANG, Liang, BINGHAM, Paul, TANAKA, Manabu, LI, Wen and KUBUKI, Shiro (2021). BiOBr/MoS2 catalyst as heterogenous peroxymonosulfate activator toward organic pollutant removal: Energy band alignment and mechanism insight. Journal of Colloid and Interface Science.

$BiOBr/MoS_2$ catalyst as heterogenous peroxymonosulfate activator toward organic pollutant removal: Energy band alignment and mechanism insight

Bofan Zhang[1, *], Mutian Zhang[2], Liang Zhang[3], Paul A. Bingham[4], Manabu Tanaka[1], Wen Li[2, *], Shiro Kubuki[1]

[1]Department of Chemistry/Applied Chemistry, Tokyo Metropolitan University, Tokyo 192-0397, Japan

[2]School of Material Science and Engineering, Ocean University of China, Qingdao, China

[3]College of Chemical Engineering, China University of Petroleum, Qingdao, China

[4]College of Business, Technology and Engineering, Sheffield Hallam University, Howard Street, Sheffield S1 1WB, UK

Abstract

Utilization of heterogenous catalysts to trigger peroxymonosulfate (PMS) activation is considered an efficient strategy for environmental decontamination. Herein, a tightly bonded flake-like 2D/2D BiOBr/MoS_2 heterojunction was successfully designed through co-precipitation process. By virtue of matched energy levels and intimate interfacial coupling, the Type-II BiOBr/MoS_2 heterojunction significantly expedited charge carrier transfer and thereby promoted the catalytic performance for organic dye oxidation and Cr(VI) reduction. The specially designed BiOBr/MoS_2 heterojunction is also conducive to split PMS and continuously generated highly active species ($SO_4^{\cdot-}$, ·OH and $\cdot O_2^-$) in a photo-Fenton system, achieving extraordinary catalytic capacity for various emerging organic pollutants (including phenol, bisphenol A and carbamazepine). The photoexcited electron with prolonged lifetime and exposed Mo sites with multivalence and multiphase nature can effectively activate PMS, which further promotes the oxidation efficiency of holes, as confirmed by scavenging experiments. The excellent stability and oxidative properties could justify scale up using BiOBr/MoS_2 to a small pilot test, implementing the potential value in practical applications. This study would provide novel insight and cognition of PMS activation via a superior heterojunction for complex polluted wastewater treatment.

Keywords: Photo-Fenton, Type-II heterojunction, Peroxymonosulfate, Reactive species, Aromatic organic pollutants

Introduction

Recent decades have witnessed increasing environmental awareness and concern regarding water pollutants caused by refractory organic pollutants and heavy metals, which pose a tremendous threat to ecological balance and human development [1, 2]. Among these, industrial dyes, phenolic compounds and hexavalent chromium (Cr(VI)) with high toxicity and carcinogenic properties are becoming urgent to be removed from water. Combinations of catalysts with electrolysis, adsorption, photocatalysis and plasma processes have been reported as useful strategies to eliminate organic contaminants and Cr(VI)). Among various pioneering strategies, peroxymonosulfate (PMS)-based advanced oxidation processes are widely considered as promising techniques for environmental purification and sustainable development through the generation of efficient sulfate radicals ($SO_4^{\bullet-}$). The formation of $SO_4^{\bullet-}$ is generally attributed from the redox recycle via cleavage of superoxide O-O bonds in the asymmetric structure of PMS by transition metal ions or carbon-rich materials [3, 4]. Owing to distinct advantages, such as wide PH range (2-9), high standard reduction potential (2.5-3.1 V) and long lifetimes in Fenton-like systems (30-40 μs), $SO_4^{\bullet-}$ has attracted extensive interest in the decontamination of refractory organic pollutants [5, 6]. In traditional photocatalytic systems, the catalytic activity can be significantly inhibited due to the swift recombination rate of hole-electron pairs. As an electron acceptor, the introduction of oxidative PMS into the photocatalysis not only accelerates the separation of photoinduced h^+-e^-, but also promotes the yield of sulfate radicals, achieving a synergistic effect for improving contaminant decomposition [7].

Thus, developing a robust and novel photocatalyst with superior catalytic performance for PMS activation is becoming a research hotspot.

Over recent decades, two-dimensional (2D) transition metal dichalcogenides (TMDs) with the general expression MX_2 (M=transition metal from IV-VII group, Mo, W; X=chalcogen, S, Se, Te) have shown great promise in energy conversion, catalysis, electronics and environmental purification [8, 9]. In the MX_2 crystal structure, the M metal atom is sandwiched by X atoms forming a monolayer, which is stacked by van der Waals forces. Especially, molybdenum disulfide (MoS_2), as a typical 2D TMD material, exhibits an indirect narrower bandgap of 1.3～1.8 eV and adjacent layer spacing of 0.61 nm in a multilayered structure [10]. Owing to the remarkable light absorption, high charge carrier density (500 $cm^2/V{\cdot}s$) and the existence of dangling bonds, MoS_2 has attracted considerable interest in the area of photocatalysis [11, 12]. Lately, it was reported that MoS_2 could accelerate Fe^{III}/Fe^{II} conversion as a cocatalyst to promote the rate-limiting step in homogenous Fenton systems [13]. Furthermore, MoS_2 can directly activate PMS to generate $SO_4^{\bullet-}$ under visible light irradiation for treating organic polluted wastewater [14, 15]. However, the inefficient PMS activation, low $SO_4^{\bullet-}$ production, and limited number of exposed active sites of MoS_2 still limit its catalytic capacity. To mitigate these drawbacks, construction of heterojunctions should be considered as a powerful strategy [16-19], which can combine the advantages of each single component and concurrently introduce certain novel properties.

As a typical family of *p*-block semiconductors, bismuth oxybromide (BiOBr)

semiconductors have been widely applied in pollutant degradation, H_2 evolution, N_2 fixation and CO_2 reduction applications [20, 21]. The spatially-anisotropic *p* state can significantly disperse the band structure, resulting in efficiently photogenerated charge carrier transfer by reducing the effective mass. Moreover, the *p* orbitals can simultaneously participate in the electronic hybridization in the conduction band and valence band position [22]. As a *p*-type material with laminated open crystal structure, BiOBr has the capacity to polarize the corresponding atoms and atomic orbitals, and then be excited by photon absorption. In the highly anisotropic crystal structure of BiOBr, $[Bi_2O_2]^{2+}$ slices are interleaved by double Br halogen atoms, resulting in fast photogenerated h^+-e^- separation and transportation in the photocatalytic process. Unfortunately, its relatively wide bandgap energy of ～3.0 eV and poor visible light absorption restrict its applications [23]. Interestingly, the wide-bandgap energy of BiOBr could match well with the relatively narrow bandgap of MoS_2 to form a staggered structure, which can absorb more photons across a wide visible light response range and effectively overcome the drawbacks of monomer molecules. Additionally, introducing PMS in such a heterogenous photo-system might bring about more benefits due to the formation of highly oxidative sulfate radicals. However, the internal electron transfer between two 2D semiconductors and the PMS activation mechanism in heterojunction/*hv* system remain ambiguous.

Therefore, in this study, BiOBr/MoS_2 heterojunction were synthesized via a facile co-precipitation process and then applied as a heterogenous PMS activator for pollutant removal. Organic dyes, phenol, bisphenol A and carbamazepine were

selected as target contaminants to explore the oxidative process, and the heavy metal Cr(VI) was chosen to study the reducibility under visible light irradiation. The main objectives of this work were as follows: (a) comparatively exploring the catalytic performance of series of BiOBr/MoS_2 composites in *hv* and PMS/*hv* systems; (b) exploring the pathways of charge carrier transfer and the dominant reactive species in both photo and photo-Fenton systems; (c) systematically investigating the active sites for PMS activation and revealing the mechanism before and after introduction of PMS. For practical applications, different polluted-wastewater conditions and scale-up experiments were also carried out. This study may provide new understanding of PMS activation via a 2D/2D heterojunction for refractory organic pollutant decontamination.

2. Experimental section

Detailed information on the materials and characterization are presented in the Supporting Material.

2.1 Synthesis of BiOBr/MoS_2 composites

The BiOBr/MoS_2 composites were synthesized through a facile precipitation method. Specifically, 1.02 g $Bi(NO_3)_3{\cdot}5H_2O$ was dissolved in 60 mL ethanol to form a homogeneous solution. Then, polyvinylpyrrolidone and an appropriate amount of MoS_2 were added into the solution with ultrasonic stirring for 60 min. Afterward, 0.1667 g KBr was introduced to the aforementioned mixture. After being stirred for another 12 h, the as-prepared grey precipitate was collected and washed. Finally, the catalysts were dried at 60℃ for 12 h. In this way, composite catalysts with different

126 MoS_2 mass ratios ranging from 1% to 8% were synthesized. Furthermore, pristine
127 BiOBr was fabricated by using the same process only without addition of MoS_2. The
128 products with 1%, 2%, 4%, 8% MoS_2 mass ratio were labeled as BMS-1, BMS-2,
129 BMS-4, BMS-8, respectively.

130 2.2 Photo and photo-Fenton catalytic activity evaluation

131 Photo or photo-Fenton catalytic oxidation and reduction activity were
132 conducted through degradation experiments using Rhodamine B (RhB), Methylene
133 Blue (MB), Methylene Orange (MO), Congo Red (CR), Phenol, Bisphenol A (BPA),
134 Carbamazepine (CBZ) and heavy metal Cr(VI) with a 100 W Hg lamp under visible
135 light irradiation. Specifically, 0.5 g/L of catalyst was added into the solution
136 containing a certain amount of pollutants. Before irradiation, the solution was
137 vigorously stirred to achieve adsorption-desorption equilibrium. During the photo or
138 photo-Fenton reaction, a 3 mL suspension was measured using UV-vis spectroscopy
139 and high-performance liquid chromatography (HPLC) to detect the concentrations of
140 residual pollutants. All experiments were repeated three times.

141 2.3 Computational parameters

142 The atomic and electronic structures of catalysts were calculated using
143 Cambridge Sequential Total Energy Package (CASTEP) software, based on density
144 functional theory (DFT) [24]. In the construction of heterostructures, to avoid
145 deformation of the electronic structure, BiOBr (001) planets with 5×5 supercells and
146 MoS_2 (002) planets with 6×6 supercells were chosen and the lattice mismatch ratio
147 was 1.58% (< 3%). The optimized layer spacing is 3.153 Å, which is in accordance
148 with the requirement of Van der Waals heterojunctions. GGA-PBE forms were used
149 for simulating the interaction between atoms [25]. The self-consistent convergence

accuracy was set at 1.0 $\times 10^{-6}$ eV per atom, and the convergence criterion for the force between atoms was 0.05 eV $Å^{-1}$. The Monkhorst-Pack mesh with K-points of 7×7×1 grid and the energy for cut-off with 350 eV were used in this simulation to improve calculation accuracy.

3. Results and discussion

3.1 Formation and characterization of 2D/2D heterojunctions

2D/2D BiOBr/MoS_2 composites were synthesized by in situ loading of ultrathin MoS_2 layers on BiOBr nanosheets via a facile coprecipitation reaction (Fig.1a). In the structure of BiOBr, Br^- can effectively suppress the stacking of $[Bi_2O_2]^{2+}$ layers by partially terminating the dangling bonds, resulting in a unique crystal structure with $[Bi_2O_2]$ slices interleaved by double Br halogen atoms [26]. The typical 2D layered transition metal sulfide (MoS_2) with a sandwiched structure was composed of a molybdenum atom layer with two hexagonally aligned sulfur layers [27]. Moreover, the tightly-bonded BiOBr/MoS_2 heterojunction with an alternating layered structure achieved by varying the doping amount of ultrathin MoS_2 layer fixed on the surface of flower-like hierarchical BiOBr, not only combined the advantages of the two single components but also drew in new superiorities.

The crystallographic structures of BiOBr, MoS_2 and BiOBr/MoS_2 composites were investigated by X-Ray Diffraction (XRD). As displayed in Fig. 1b, diffraction peaks of pure BiOBr nanosheets corresponded closely to single-phase tetragonal BiOBr (001), (002), (101), (102), (110), (112), (200) and (212) planes (JCPDS card No. 73-2061, a=3.926 Å, b=3.926 Å, c=8.103 Å) [28]. Pristine MoS_2 exhibited a

sharp characteristic peak at 13.8° and a broader peak at 33.3° , which were indexed to (002) and (100) planes, respectively. For the BiOBr/MoS_2 composites, the diffraction peaks of BiOBr were clearly observed, indicating that introduction of MoS_2 did not influence the original crystal structure of BiOBr. However, the characteristic peaks of MoS_2 are not apparent in the XRD pattern except the peak located at 13.8°, which is mainly attributed to the low loading ratio and high dispersion of MoS_2 nanolayers [29]. In the FT-IR spectra (Fig.S2), the distinct bond of BiOBr was clearly detected in the BiOBr/MoS_2 composites, indicating that the chemical structure of BiOBr was still retained after combining with MoS_2. The morphology and microstructure of BiOBr, MoS_2 and BiOBr/MoS_2 composites were characterized and shown in Fig.1c-h. For pristine BiOBr, the flower-like structures were comprised of numerous finely BiOBr layers and the average particle size was ~2 μm. Similarly, pure MoS_2 also displayed a uniform and spherical structure with numerous nanosheets. Generally, ultrathin 2D nanosheets could expose adequate active sites and accelerate charge carrier transfer by reduced charge diffusion lengths [30]. With increasing content of MoS_2 nanosheets (NSs), the flower-like hierarchical structure of BiOBr was gradually destroyed and exhibited stacked flake-like features, which is mainly attributed to the intercalation effect between two 2D nanolayers materials [31, 32]. The TEM images of BiOBr/MoS_2 composites further confirmed the tightly stacked structure by layered aggregation of nanosheets (Fig.1i-k). The continuous interplanar spacing of 0.277 and 0.65 nm in BMS-2 matched perfectly to the (001) and (002) facets of BiOBr and MoS_2, respectively. TEM energy-dispersive X-ray spectroscopy (TEM-XEDS

mapping) with spatial distribution of Bi, O, Br, Mo and S (Fig.1l) illustrated the homogeneous formation and the closely-bonded BiOBr/MoS_2 catalyst. X-Ray Photoelectron spectra (XPS, Fig.S3) clearly demonstrated the Mo, S, Bi, O and Br elements in the BMS-2 composite, and the Bi/Mo atomic ratio was similar to the experimentally theoretical value. In summary, all of these results revealed the successful construction of 2D/2D heterojunction between the BiOBr and MoS_2 components.

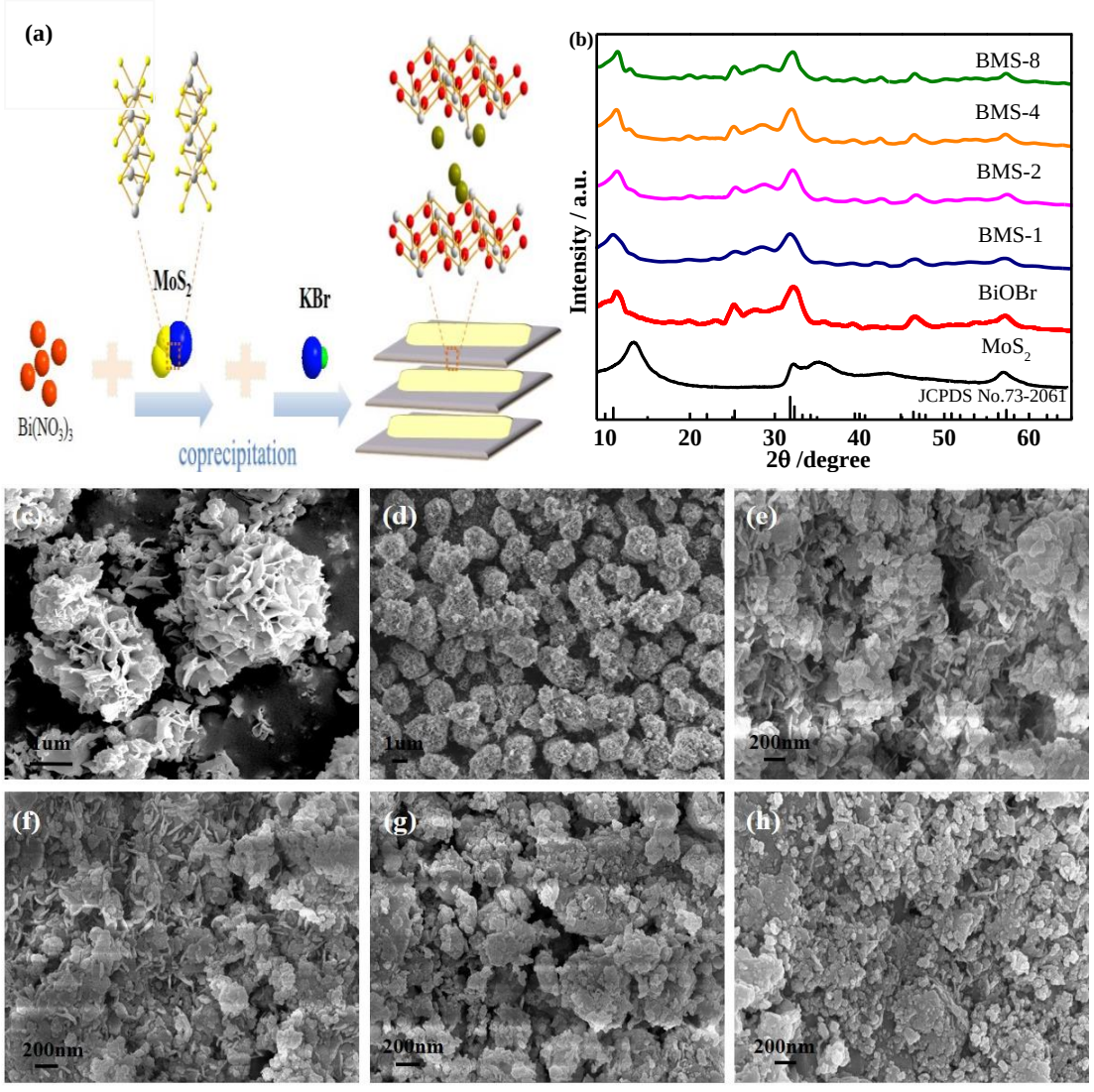

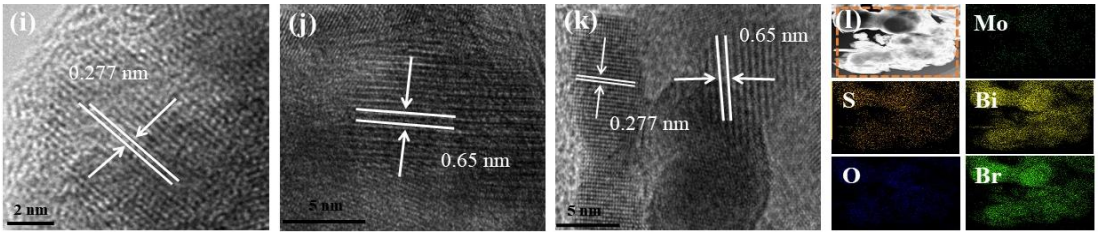

Fig. 1 (a) Schematic diagram of fabrication procedure of $BiOBr/MoS_2$ catalyst; (b) XRD patterns, (c-h) SEM images of BiOBr, MoS_2, BMS-1, BMS-2, BMS-4 and BMS-8, the scale bar were 1μm in (c-d) and 200 nm (e-h); (i-k) TEM image of BiOBr, MoS_2 and BMS-2, the scale bar were 2 nm, 5 nm and 5 nm; (l) Energy-dispersive X-ray spectroscopy mapping (STEM-XEDS) of BMS-2 catalyst.

3.2 Catalytic ability towards various aromatic organic pollutants and heavy metal

The oxidative and reductive performances of $BiOBr/MoS_2$ catalysts were investigated via decomposition of RhB and heavy metal Cr(VI) under visible light irradiation (Fig.2) after reaching adsorption-desorption equilibrium (Fig.S4). Impressively, the $BiOBr/MoS_2$ composites showed a higher catalytic activity for RhB oxidation (Fig.2a) and Cr(VI) reduction (Fig.2e) compared with pristine BiOBr, which may be due to the strong closely-bonded effect and promoted separation of charge carriers between MoS_2 and BiOBr. Among these catalysts, BMS-2 exhibited the highest catalytic efficiency and the catalytic variation of $BiOBr/MoS_2$ hybrids followed a volcano curve tendency with increasing dopant content of MoS_2 from 0 to 8 %, implying that interfacial coupling between MoS_2 and BiOBr is a crucial factor. It is proposed that when MoS_2 content is lower than the optimum content, the MoS_2/BiOBr composite has fewer adsorption and trapping sites for carriers, resulting in acceleration carriers recombination and shortening the carrier survival time [33].

On the contrary, excessive MoS_2 would hinder the interfacial contact between BiOBr and MoS_2, leading to agglomeration of nanosheets, and eventually provoking a light shielding effect on the catalyst surface. Therefore, at optimal doping levels, MoS_2 not only exposed sufficiently reactive sites but also provided more coupling sites at the interface for photogenerated carrier transfer, which achieved the best synergistic effect during the catalytic process. All of the apparent constant values (*k*) can be fitted well with pseudo-first-order kinetics, not only in oxidation processes but also in reduction processes (Fig.S5). Besides, the long-term and repeated cycling experiments (Fig.S6) proved that BMS-2 possessed photostability under decontamination processes.

The photo-Fenton catalytic performance of BiOBr/MoS_2 was further explored by degradation of different organic dyes under visible-light-assisted PMS activation (Fig.2b, f). Notably, under photocatalysis without PMS conditions, only 52.8% of RhB was removed after 10 min (Fig.2a), a removal rate which is much lower than that of the photo-Fenton reaction in the presence of peroxymonosulfate (86.8%), indicating the essential role of PMS in accelerating the catalytic process. Similarly, the introduction of PMS also displayed excellent oxidative ability for various organic dyes, in which the MB, MO and CR degradation efficiencies of 94.1, 93.4 and 85.3% were respectively achieved after 20 min (Fig.2f). Compared with the photocatalytic system, the addition of PMS obviously promoted the apparent rate constant, which is 2.13 time higher than the photo-system (Fig.2c). It is clearly demonstrated that PMS can be efficiently activated via BiOBr/MoS_2 and visible light, resulting in fast separation of photo-induced charge carriers and generation of more effective reactive

oxygen species during the catalytic process. The further mineralization rate of a series of organic dyes by BMS-2 in the PMS/*hv* system were explored through total organic carbon (TOC) analyses. As shown in Fig.2d, the TOC removal efficiency for organic dyes could reach 52.2, 48.3, 53.9 and 43.6%, respectively, and the mineralization rate of RhB still remained 49.0% after four cycles, illustrating the outstanding oxidisability and stability under a visible-light-activated PMS system.

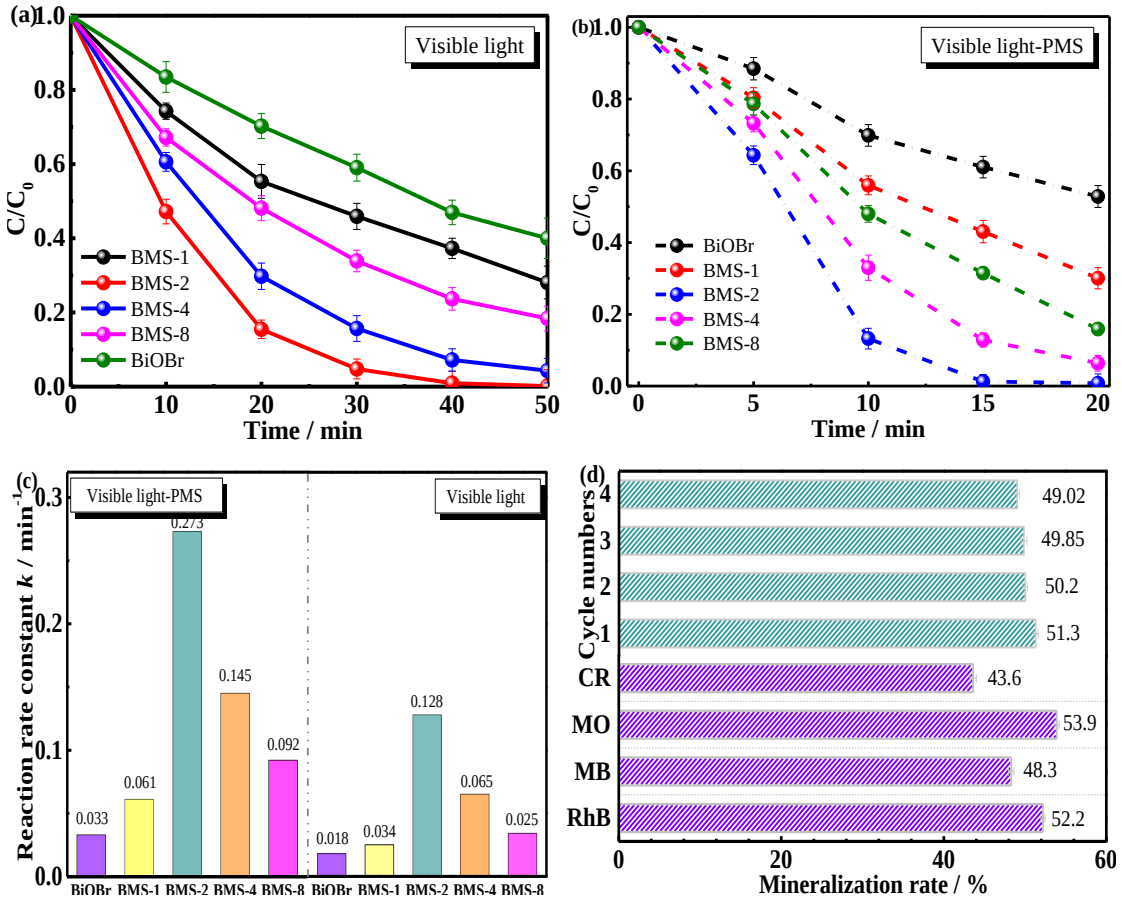

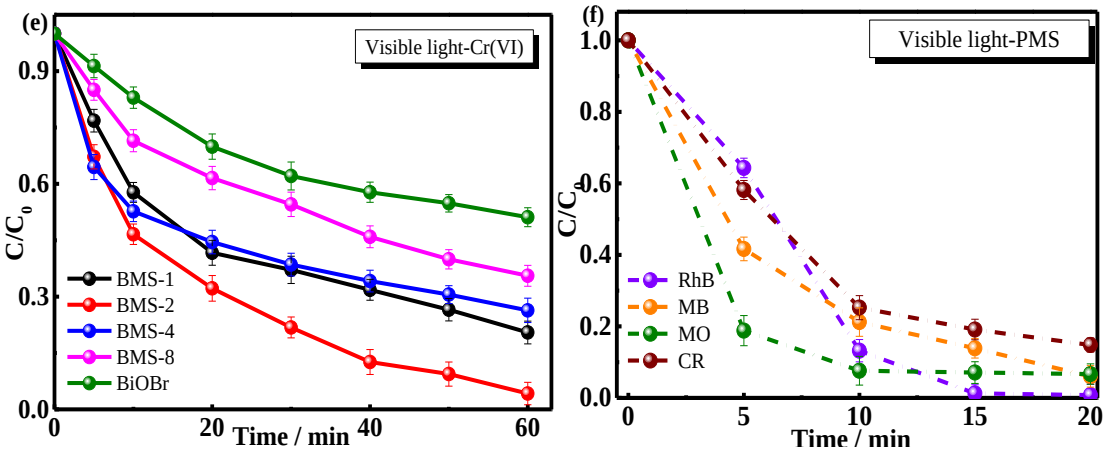

Fig. 2 The decomposition of RhB under the visible light irradiation (a), under visible light assisted PMS activation (b), (c) Reaction rate constant in photo and photo-Fenton system via the prepared catalysts; (d) Mineralization efficiency of organic dyes (RhB, MB, MO, CR) in BiOBr-MoS_2/PMS/*hv* system; (e) The reduction of Cr(VI) under visible light irradiation via the prepared catalysts; (f) The degradation of different organic dyes under BiOBr-MoS_2/PMS/*hv* system. Reaction conditions: catalyst=0.5 g/L, [PMS]=1 mM (photo-Fenton), pollutants=20 mg/L.

3.3 Effect of parameters on removal of organic dyes by activation of PMS

To achieve optimal parameters during the PMS activation reaction, the effects of pH, PMS concentration, catalyst dosage and several inorganic anions in actual wastewater were investigated (Fig.3 and Fig.S7). The pH is considered a sensitive factor due to the fact that it significantly influences the interactions between catalyst, pollutants and PMS. As shown in Fig.3a, it was noted that too high and too low pH values are not helpful for degradation efficiency. This is due to the affinity between H^+ and HSO_5^- having an adverse effect and $SO_4^{\bullet-}$ could convert into •OH under basic conditions, while $SO_4^{\bullet-}$ was the major reactive oxygen radical in the PMS activation process [34]. Furthermore, when under alkaline conditions, the edge S cannot be captured, thus inhibiting the exposure of Mo (IV) to participate in the reaction [35].

Although the degradation capacity somewhat decreased with higher and lower pH values, it can also achieve stable catalytic activity across an extensive pH range and exhibit a highest catalytic activity at PH=6.5. Therefore, pH=6.5 was chosen as an optimal value for the following reaction. Afterward, the effect of PMS concentration was explored and is illustrated in Fig.3b. It was found that the degradation rate gradually improved with increasing PMS dose from 0.5 to 10 mM. This contributed to the generation of more reactive oxygen radicals under higher PMS concentrations. Nevertheless, there is no significant improvement between 1 mM (98.7%) and 5 mM (99.0%) after 15 mins. Given the trade-off between catalytic activity and cost, the PMS concentration was fixed at 1 mM. The influence of catalyst dosage was also evaluated and was depicted in Fig.3c. Generally, more active sites can be exposed with an increased dose of catalyst, and eventually enhance the decomposition rate of pollutants. As expected, the degradation rate dramatically improved from 68.2% to 98.8% with the amount of catalyst increased from 0.1 to 0.5 g/L. Upon further increasing the dosage (> 0.5 g/L), no significant enhancement was observed after 15 min reaction. Considering the effects of light scattering and aggregation by excessive catalysts, the optimal catalyst dosage was chosen as 0.5 g/L. In practical applications, inorganic anions are abundant in the actual water and easily react with the generated reactive radicals, eventually affecting the degradation efficiency [36]. To better evaluate the actual application potential of BiOBr/MoS_2 catalysts, the effects of three representative inorganic anions (Cl^-, HCO_3^- and NO_3^-) on the catalytic performance were systematically explored. As displayed in Fig. 3d-f, Cl^- had an inhibiting effect on

the catalytic activity in the range of 1 mM～10 mM, which might be ascribed to the interaction between Cl^- and $SO_4^{\bullet-}$ ($Cl^-+SO_4^{\bullet-}\rightarrow Cl^{\bullet}+SO_4^{2-}$; redox potential: $Cl^{\bullet}$ 2.4V, $SO_4^{\bullet-}$ 2.5-3.1V) [37], resulting in significant consumption of highly oxidative sulfate radicals and thus suppression of the catalytic reaction. Similarly, the HCO_3^- had an obviously inhibitory effect even at low concentrations (1mM). Owing to the fact that HCO_3^- could neutralize H^+ in the reaction system, the edge S atoms in MoS_2 cannot be easily captured and the activation of PMS by Mo (IV) was significantly suppressed. The introduction of NO_3^- also produces a negative influence due to the generated lower oxidation ability radical $NO_3^{\cdot}$ by the $SO_4^{\bullet-} + NO_3^-\rightarrow NO_3^{\bullet} + SO_4^{2-}$ reaction [36]. Therefore, all three common inorganic anions have an adverse effect on the PMS/*hv* system, which were not conducive for compound removal.

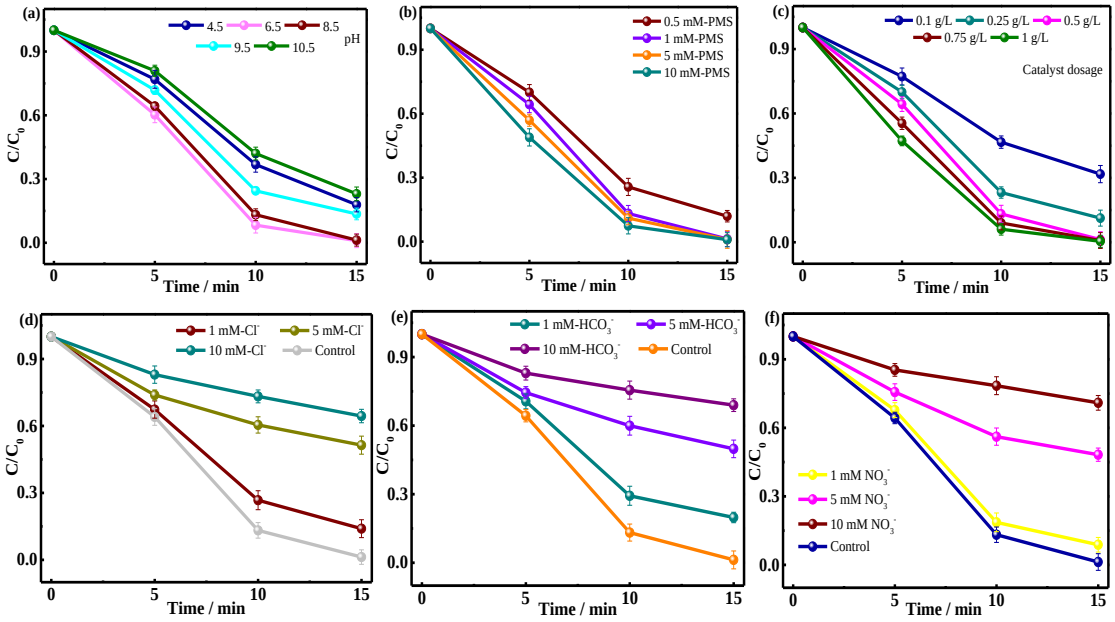

Fig. 3 Different influencing factors of the BMS-2 catalyst for the degradation of RhB in the PMS/*hv* system (a) pH value (PMS concentration:1mM, Catalysts dosage: 0.5g/L); (b) PMS concentration (pH=6.5, Catalysts dosage: 0.5g/L); (c) Catalyst dosage (pH=6.5, PMS concentration:1mM); (d-f) Various ions including Cl^-, HCO_3^- and NO_3^- (pH=6.5, PMS

concentration:1mM, Catalysts dosage: 0.5g/L); The PH value was regulated using NaOH and H_2SO_4 (0.1M) solution.

3.4 Catalytic mechanism of BiOBr/MoS_2 heterojunctions

Considering the promoted catalytic capacity of BiOBr/MoS_2 composite and the further improved efficiency via introduction of PMS, a series of systematic explorations was performed to reveal the internal coupling mechanism between the two materials and PMS. Firstly, to clarify the charge carrier transfer and separation behaviors during the catalytic process, electrochemical impedance spectroscopy (EIS), photoluminescence (PL) spectroscopy and photocurrent response measurements were carried out. As shown in Fig.4a, pure BiOBr exhibited a strong emission peak at about 470 nm due to the band edge transition and the rapid recombination rate. As expected, the peak intensity of BiOBr/MoS_2 composite was significantly weakened after integrating with MoS_2 ultrathin nanosheets, implying the boosted generation yield of reactive species and the suppressed photoinduced e^--h^+ recombination efficiency. Additionally, BiOBr/MoS_2 hybrid plots had a much smaller radius than for pristine BiOBr and the interfacial resistance for sample BMS-2 was smallest (Fig.S8a), indicating the rapid charge carrier mobility from the BiOBr/MoS_2 electrode to the solid/liquid interface. This may be attributed to the higher conductivity of MoS_2 in composites, which favor charge carrier transfer during the catalytic process [38]. Similarly, the BiOBr/MoS_2 composites displayed higher photocurrent density than pure BiOBr (Fig.S8b), and the BMS-2 exhibited the highest value, illustrating the inhibited recombination rate of photo-excited carriers due to the well-constructed

bonded interface. The improved electron transfer and decreased carrier resistance in BMS-2 are also beneficial for the activation of PMS. Therefore, charge carrier transfer between solid catalyst interface and solution containing PMS were investigated by EIS and photocurrent response. As displayed by the highest photocurrent density and smallest arc radius (Fig.4b-c), the BMS-2/PMS system exhibited a faster photoinduced electron-hole separation and carrier transfer, mainly ascribed to the role of electron acceptor of PMS and PMS activation through catalyst surface active sites in the photo-Fenton system.

Owing to the semiconductor characteristics of BiOBr and MoS_2, and the improved catalytic efficiency of BiOBr/MoS_2 composites under visible light irradiation, the optical properties and band structure were studied by UV–vis diffuse reflectance spectroscopy (DRS) and Mott-Schottky measurement. As shown in Fig.4d, the UV-vis DRS of BiOBr/MoS_2 composites presented enhanced absorption ranging from 450-700 nm compared to pure BiOBr, illustrating efficient interfacial charge carrier mobility by the gradually shortened transition distance between BiOBr and MoS_2, and improved luminous energy-harvesting ability. The bandgap energies (E_g) of BiOBr and MoS_2 were calculated as 2.93 and 1.29 eV, respectively (Fig.S9), via a plot using the Kubelka-Munk (K-M) method [39]. According to the equation $E_{VB} = E_g + E_{CB}$, the corresponding valence band and conduction band potentials of BiOBr and MoS_2 were calculated to be 2.42, -0.51 eV and 0.67, -0.62 eV, respectively, versus the normal hydrogen electrode (NHE), respectively (Fig.S9). The more negative minimum CB edge of MoS_2 than BiOBr and more positive maximum VB edge of

BiOBr than MoS_2 enable them to form a staggered bandgap structure, which is conducive to charge carrier separation and migration.

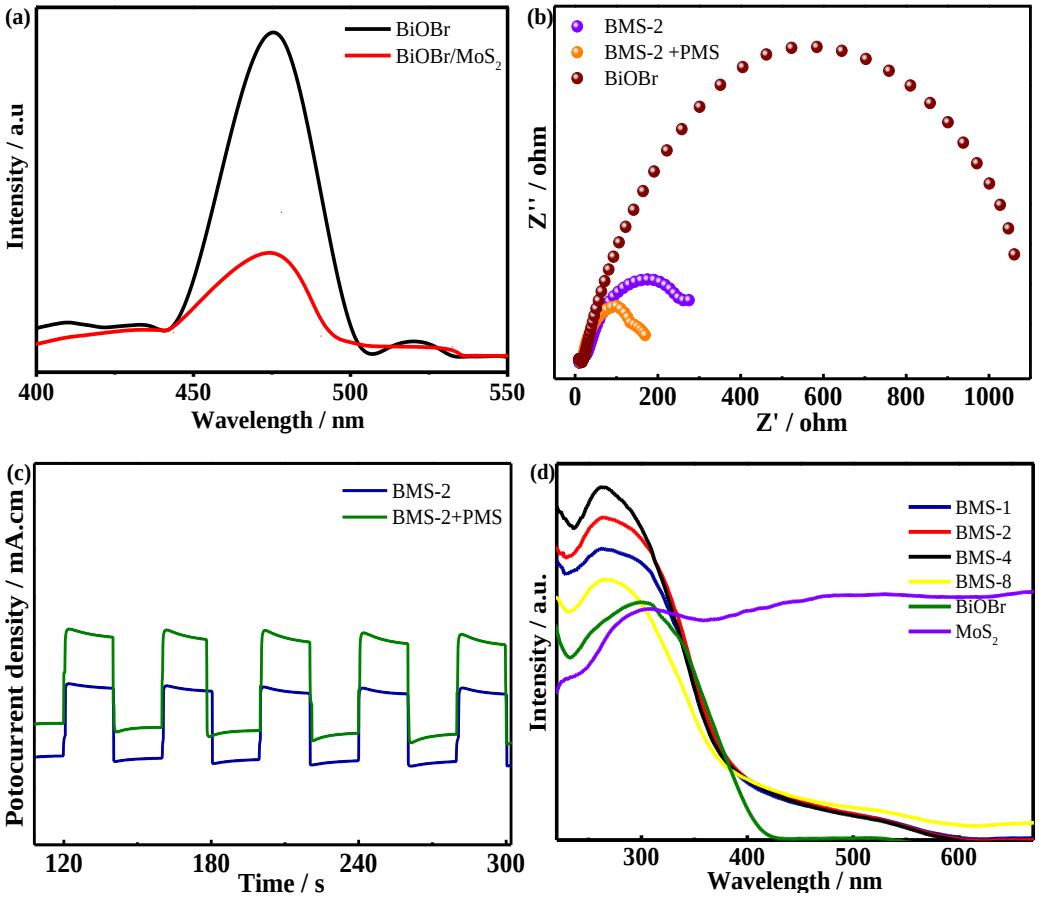

Fig.4 (a) Photoluminescence (PL) spectra of BiOBr and BMS-2; (b) EIS spectrum and (c) Transient photocurrent response and before and after addition of PMS via BMS-2; (d) UV-vis DRS and Plots of the $(ahv)^2$ *vs* photon energy(hv) of synthesized catalysts

To acquire the pathway of charge carrier transfer, the reactive species generated by BMS-2 were investigated by adding various scavengers under photocatalytic reaction without PMS. As exhibited in Fig.5a, in comparison with no-scavenger conditions, the addition of TEOA (scavenging for h^+) or BQ (scavenging for $\cdot O_2^-$) provoked significant deactivation of the BMS-2 catalyst, with inhibition rates of ~48.8% and ~54.6% toward RhB decomposition, respectively. This result

demonstrated that h^+ and $\cdot O_2^-$ are the major active radicals in the photocatalytic reaction. However, in the presence of IPA (Isopropanol, scavenging for ·OH), the degradation rate was not obviously affected and was still maintained at a high value, indicating that ·OH played a modest role. To further interrogate this result, electron paramagnetic resonance (EPR) with 5,5-dimethyl-1-pyrroline N-oxide (DMPO)-CH_3OH as a spin-trapping agent was selected to measure $\cdot O_2^-$ active species under visible light illumination. The typical signal of DMPO-$\cdot O_2^-$ ((a_N=14.9G, a^{α}_H=10.38G and a^{β}_H=1.31G)) [40] were clearly observed and the intensity was gradually enhanced by the extension of irradiation time, which clearly validated the formation and critical role of superoxide radicals ($\cdot O_2^-$) in the BiOBr/MoS_2/*hv* system.

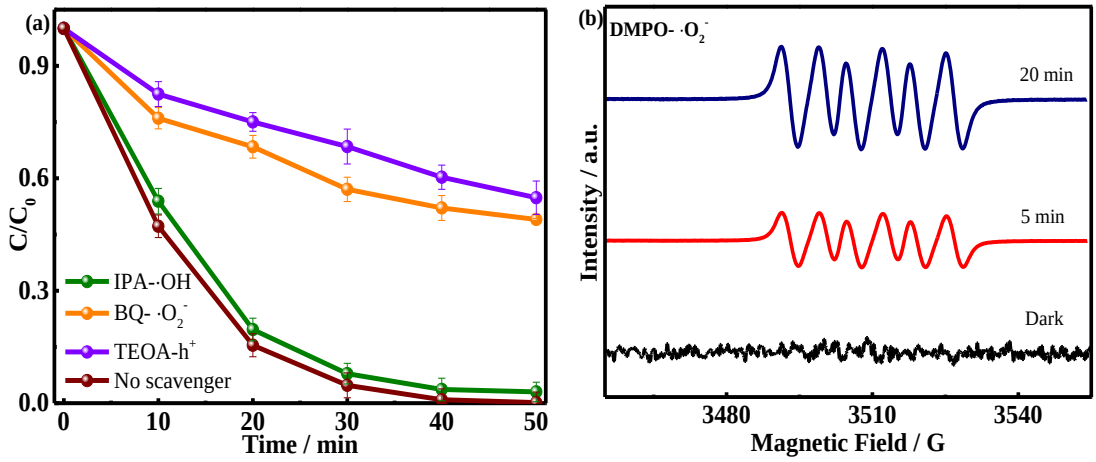

Fig.5 (a) Scavenging experiment for ·OH, $\cdot O_2^-$ and h^+; (b) EPR spectra of DMPO- $\bullet O_2^-$ for BMS-2 catalyst only under visible light irradiation

To further reveal the mechanism of enhanced carrier transfer and catalytic activity, DFT calculations were applied and simulated for the structure and properties of BiOBr/MoS_2 heterojunctions. As shown in Fig.6, in comparison with the work function (W_f) along with the interface of pristine BiOBr (6.079 eV) and MoS_2 (5.807 eV), the W_f of BiOBr/MoS_2 heterojunctions decreased to 4.941eV due to the electric

field and strong coupling built into the interface, which could significantly inhibit recombination and increase charge carrier mobility. The energy band structure of the material is a crucial factor, reflecting its ability to utilize photogenerated electrons and holes [41]. As depicted in Fig.6d, BiOBr and MoS_2 are both indirect semiconductors and the band-gap values are about 2.71 and 1.62 eV. The calculated band-gap of BiOBr was slightly lower than the experimental value due to underestimation by GGA-PBE functional analysis [42]. On the contrary, the calculated value for MoS_2 was a little higher than the experimental data but lower than for monolayer MoS_2, which is consistent with the previous conclusions based on GGA-PBE calculations [43]. As a direct semiconductor, the band-gap energy of BiOBr/MoS_2 catalyst is about 1.03 eV and is lower than for pure materials, owing to the closely-bonded interaction and successful formation of heterojunctions. Generally, the indirect band-gap property is unfavorable for carrier migration and energy can be lost in the form of phonons during transfer between valence band and conduction band. Herein, the direct BiOBr/MoS_2 heterojunction significantly promotes the utilization of energy and catalytic efficiency compared to pristine BiOBr and MoS_2 with direct band-gaps. Furthermore, light absorption is an additional vital measure of catalytic efficiency, which is determined by the real and imaginary parts of dielectric constant. The related formulas are expressed as follows:

$$\varepsilon(\omega) = \varepsilon'(\omega) + i\varepsilon''(\omega) \quad (1)$$

$$I(\omega) = \sqrt{2}\omega[\sqrt{\left(\varepsilon'(\omega)\right)^2 + \left(\varepsilon''(\omega)\right)^2} - \varepsilon'(\omega)]^{1/2} \quad (2)$$

It can be noted that the light absorptivity (I) is mostly affected by the imaginary

part (ε'). As shown in Fig.6c, the structure of the heterojunction exhibited strong absorption ability at visible and near-infrared wavelengths, and the main absorption peak (at about 2.3 eV) is located in the energy range of visible light (1.76-3.11 eV), implying good performance of heterojunction structures in real-world service environments. In addition, the band edge position of BiOBr/MoS_2 was still more negative than that of superoxide radical potentials (-0.33 eV), which possess excellent oxidative capacity under visible light radiation.

Based on the above analysis, the pathway of photoexcited carriers in photo-systems followed a Type-II band alignment transfer. Specifically, both BiOBr and MoS_2 can be excited and generate e^- and h^+ under visible light illumination. An internal electric field was correspondingly formed in the constructed BiOBr/MoS_2 composite, leading to the transport of e^- from the CB of MoS_2 to BiOBr, with the migration of h^+ from the VB of BiOBr to MoS_2, which exhibited a Type-II charge migration mechanism. The strong interfacial coupling could induce fast carrier transfer and then efficiently adsorb the organic substrates to be decomposed. Due to the more negative conduction band energy (-0.51 eV) of BiOBr than that of $O_2/\cdot O_2^-$ (-0.33 eV), photogenerated electrons can absorb the oxygen (O_2) and then reduce it to highly active $\cdot O_2^-$ radicals. Afterward, active $\cdot O_2^-$ and h^+ species with remarkable oxidative potential could degrade various aromatic organic contaminants into small molecules. Moreover, photoexcited electrons and exposed Mo(IV) reducing sites could simultaneously participate in the catalytic reduction (Cr(VI) → low toxic Cr(III)), resulting in superior photocatalytic oxidic-ability and reducibility of

BiOBr/MoS_2 catalyst.

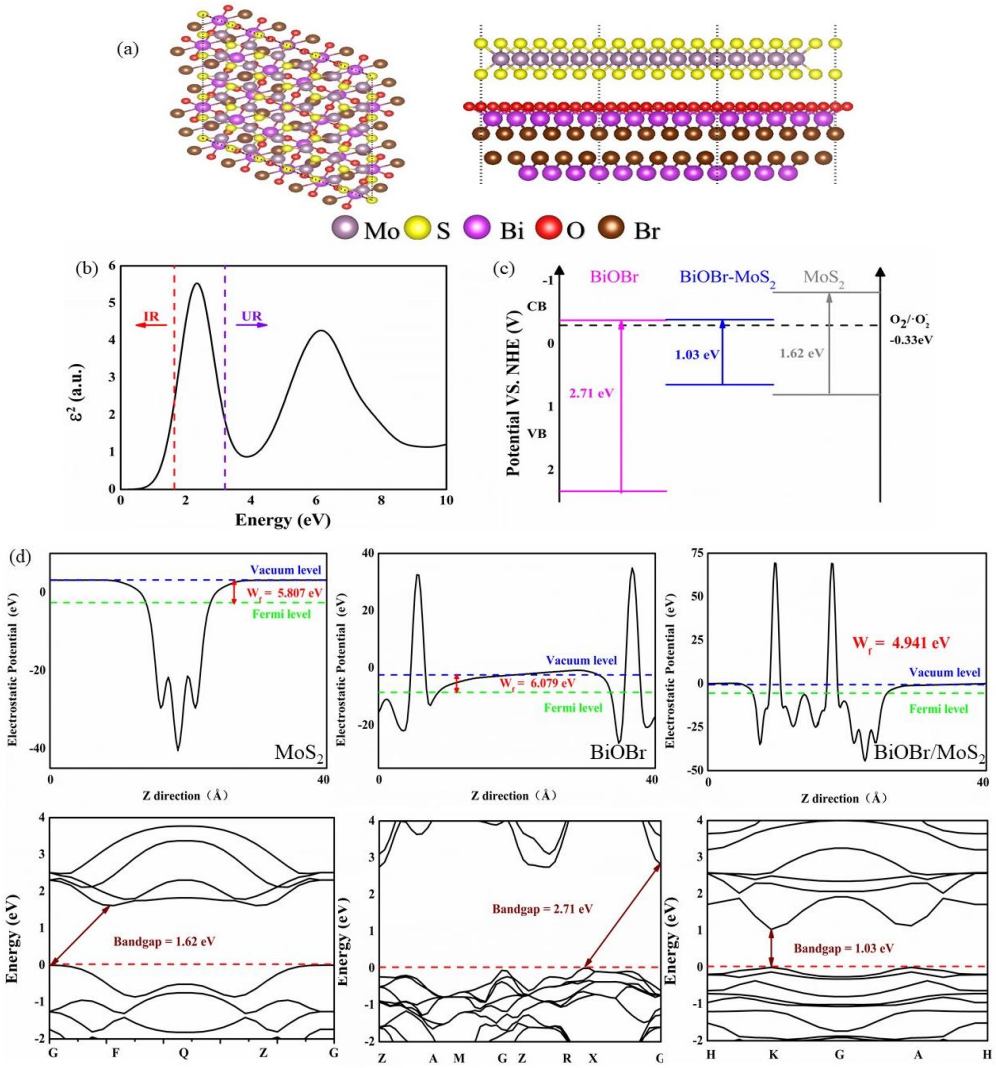

Fig.6 (a) Top-view and side-view of BiOBr/MoS_2 heterojunction; (b) Dielectric constant imaginary part (IR: infrared region and UR: ultraviolet region); (c) Band edge position of·O_2^- of BiOBr, MoS_2 and BiOBr/MoS_2 catalysts; (d) Electronic potential drop and energy band structure of MoS_2, BiOBr and BiOBr/MoS_2 catalyst.

After introduction of PMS into the BiOBr/MoS_2/*hv* system, the oxidative performance further improved. To investigate the main oxidative species in BiOBr/MoS_2/*hv*/PMS system, electron paramagnetic resonance (EPR) spectra were acquired with the help of 5,5-dimethyl-pyrroline N-oxide (DMPO) agent. As shown in

Fig.7a, the EPR spectra of DMPO-·OH (aN=14.9G, aH=14.9G) and DMPO-$SO_4^{\cdot-}$ (aN=13.2G, aH=9.6, 1.48 and 0.78G) [44] can be clearly detected after 10 min with visible light irradiation and introduction of PMS, demonstrating that $SO_4^{\cdot-}$ and ·OH were both involved in the PMS/*hv* system. Besides $SO_4^{\cdot-}$ and ·OH, a weak characteristic signal of $^1O_2$ was observed via the triplet EPR spectra using 2,2,6,6-tetramethylpiperidine (TEMP) as a spin-trapping agent (Fig.7b). Noting that the densities of $SO_4^{\cdot-}$ and ·OH were much higher than $^1O_2$, it can be deduced that $SO_4^{\cdot-}$ and ·OH played major roles in the BMS-2/PMS/*hv* system. To further quantitatively analyze the effects of $SO_4^{\cdot-}$ and ·OH radicals, the sacrificial agents methanol and tert-butanol (TBA) were added. Generally, methanol can capture both hydroxyl radicals ($k_{methanol/\cdot OH}$ =1.5～2.5×10^9 $M^{-1}s^{-1}$) and sulfate radicals ($k_{methanol/SO4\cdot-}$ =1.5～7.5×10^7 $M^{-1}s^{-1}$). For the sacrificial agent of TBA, it also could react with both hydroxyl radicals ($k_{TBA/\cdot OH}$ =3.5～7.5×10^8 $M^{-1}s^{-1}$) and sulfate radicals ($k_{TBA/SO4\cdot-}$ =4.0～9.0×10^5 $M^{-1}s^{-1}$) [35]. However, due to the reaction constant of ·OH being far higher than for $SO_4^{\cdot-}$, the sacrificial effect on $SO_4^{\cdot-}$ by TBA can be ignored. Moreover, owing to the fact that $SO_4^{\cdot-}$ can be easily transformed into •OH via equation 3, to determine the dominant reactive radicals in the PMS/*hv* system, TBA and methanol were both added. As shown in Fig. 7c, the degradation efficiency was inhibited 19%/50% when 0.05 M TBA/methanol was introduced into the system, respectively. It can be inferred that the calculated ratio of $SO_4^{\cdot-}$ to ·OH was about 2.6:1, indicating that $SO_4^{\cdot-}$ could provide more contribution to the degradation rate than that of ·OH. As the methanol concentration increased to 0.5 M, the removal rate further decreased

462 to 31.2%, illustrating the significant role of sulfate radicals in the decomposition of

463 organics.

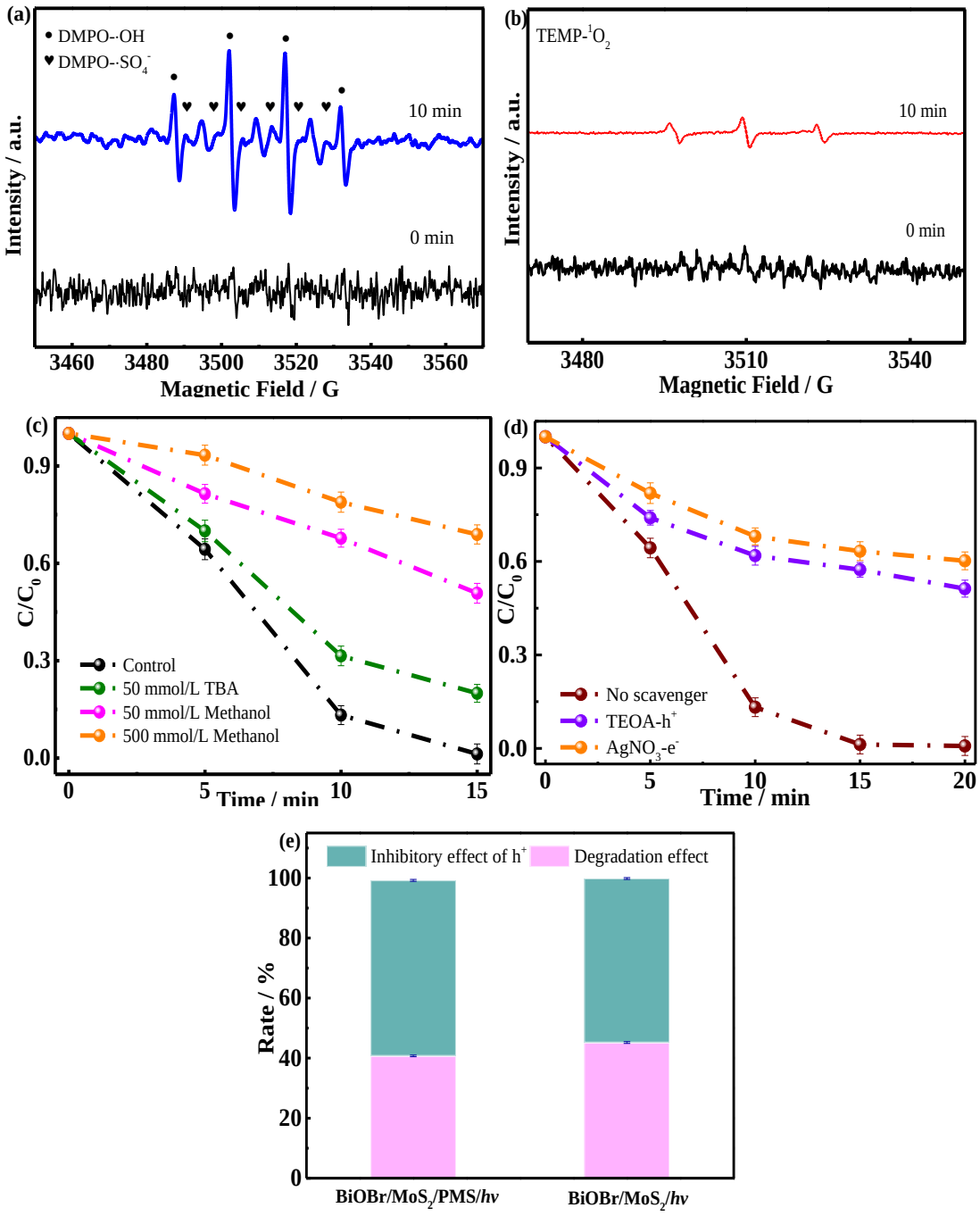

464

465

466

467 Fig.7 (a) EPR spectra of DMPO-·OH and $SO_4^{\cdot-}$, (b) EPR spectra of TEMPO-$^1O_2$, (c) Effects of

468 TBA and methanol on the removal of pollutant, (d) Effect of h^+ and e^- in the BiOBr-MoS_2/PMS/*hv*

469 system and (e) Inhibitory effect of h^+ before and after addition of PMS. Reaction conditions:

470 catalyst=0.5 g/L, [PMS]=1 mM (photo-Fenton), pollutants=20 mg/L.

In the process of PMS activation, PMS can not only act as an electron acceptor and then convert to $SO_4^{\bullet-}$ and ·OH (equation 4), but also as an electron donor to produce $^1O_2$ (equations 5 and 6) [45]. To reveal the internal reactive mechanism in the BiOBr/MoS_2 system, quenching experiments were conducted using triethanolamine (TEOA) and $AgNO_3$ as h^+ and e^- quenchers, respectively. As depicted in Fig.7d, in the presence of TEOA or $AgNO_3$, an obvious inhibitory effect on pollutant degradation was observed, implying that both PMS and visible light made a contribution to the catalytic process. In comparison with holes, the electrons played a more important role in the BiOBr/MoS_2/PMS/*hv* system, indicating that the majority of e^- participated in the process of PMS activation. Furthermore, the inhibitory effect of holes before and after addition of PMS was also explored. After introduction of PMS and TEOA, the oxidative effect of holes was improved (Fig.7e), which is attributed to the consumption of e^- by PMS and more efficient separation of photoinduced h^+-e^- pairs. These results indicate that more photoexcited electrons were transferred to the electron acceptor of PMS and then facilitated the generation of $SO_4^{\bullet-}$ and ·OH radicals, which was consistent with the EPR analysis.

$$SO_4^{\bullet-}+H_2O\rightarrow SO_4^{-}+\cdot OH+H^+ \quad (3)$$

$$PMS(HSO_5^-)+e^-\rightarrow SO_4^{\bullet-}/\cdot OH \quad (4)$$

$$PMS(HSO_5^-)-e^-\rightarrow SO_5^-+H^+ \quad (5)$$

$$SO_5^-+H_2O\rightarrow HSO_4^-+{}^1O_2 \quad (6)$$

It is known that transition metal sulfide MoS_2 with multiphase (1T/2H) and multivalent molybdenum (IV, V and VI) can effectively activate PMS conversion and

maintain a persistent Fenton-like reaction by the stable active sites [15]. Moreover, the radicals formed via PMS activation undergo an electron transfer process, while the corresponding metal ion can be transformed from low valence to high valence, such as Fe, Co, Cu and Mn [46, 47]. Similarly, benefiting from the above-mentioned merits, transition metal Mo ion sites may play an essential role in PMS activation and radical generation in the PMS/*hv* system for organic pollutant removal. Herein, to clarify whether and how phase and valence variations happened, high resolution XPS spectra of Mo 3d before and after reaction were measured. As shown in Fig.8a, four characteristic peaks appeared at 228.27, 229.15, 231.44 and 232.37 eV and were identified to 1T and 2H phases of Mo(IV) $3d_{5/2}$ and Mo(IV) $3d_{3/2}$, respectively. Correspondingly, the ratios of two phase (1T/2H) were estimated to be 5.86 and 1.88 via the deconvolution of Mo XPS signals. Generally, the coexistence of 1T/2H phases in MoS_2 favors the light response that occurred in the 2H phase and the catalytic behavior occurred in the 1T edge sites. Due to the 1T phase being an active phase, the high content of 1T is conducive to PMS adsorption with high adsorption energy and promote the PMS cleavage with low Gibbs free reaction energy [15]. Notably, treated by an amount of PMS, the ratio of 1T/2H phases for the used MoS_2 decreased to 3.66 and 1.72, and a small fraction of Mo(VI) located at 235.39 eV emerged in the Mo 3d spectra. This phenomenon implied that active 1T phase participates in the reaction and partial low-valence Mo(IV) was transformed to Mo(VI) during PMS activation, which is a favorable configuration for BiOBr/MoS_2 catalysts for decomposing pollutants. However, no obvious Mo(V) was observed after reaction, which is ascribed to the

rapid conversion from Mo(IV) to Mo(V) and further oxidation to Mo(VI). This phenomenon validated that Mo(IV) in heterojunctions is an essential active site for PMS activation.

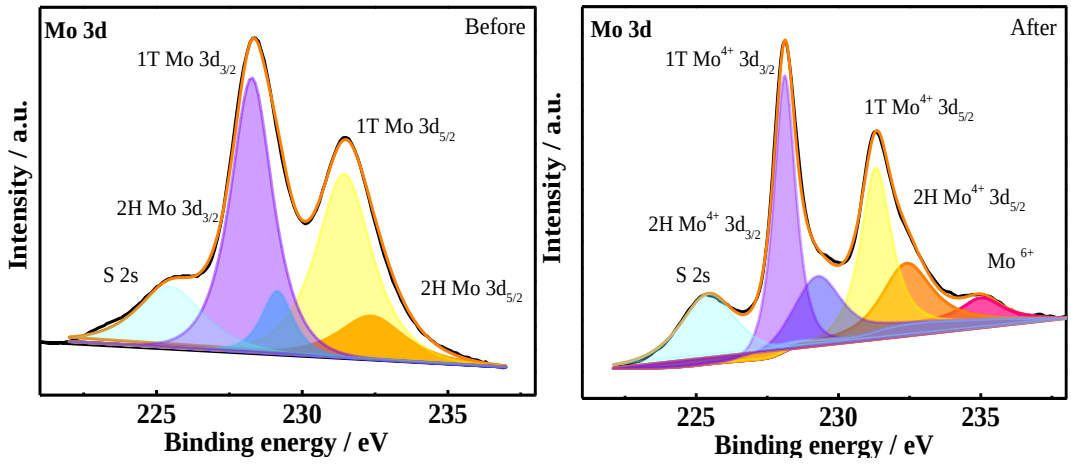

Fig.8 High resolution of XPS spectra of Mo 3d in BiOBr/MoS_2 before and after PMS activation under visible light illumination

On the basis of above characterizations and analysis, a plausible mechanism for BiOBr/MoS_2 heterojunctions with PMS activation was proposed, as shown in Fig.9. In the BiOBr/MoS_2/*hv* system, the constructed closely-bonded 2D/2D Type-II heterojunction augmented charge separation as well as inhibited the photoinduced h^+-e^- recombination. The CB potential of BiOBr is more negative than the standard redox potential of O_2/•O_2^-, which means that e^- in CB of BiOBr can reduce O_2 to generate • O_2^- radicals to directly oxidize the pollutants. After addition of peroxymonosulfate, the photo-induced electrons can be trapped by PMS (as an electron acceptor) and then converted into $SO_4^{\bullet -}$, resulting in more efficient h^+-e^- separation and carrier transfer, as confirmed by photocurrent response and EIS measurement [48]. The remaining h^+ in the heterojunction correspondingly manifest

improved oxidative capacity compared with photocatalysis. Simultaneously, the PMS can be also activated by Mo(IV) into $SO_4^{\bullet-}$ and Mo(IV) transformed into high-valent Mo(VI) species. The formed diffusible $SO_4^{\bullet-}$ could further yield •OH via an interconversion ($SO_4^{\bullet-}+H_2O \rightarrow SO_4^{-}+ \bullet OH+H^+$) and participate into the oxidation process. Besides, the Mo(IV) with low valence can reduce Cr(VI) into low toxicity Cr(III) [49], which gave a synergistic effect with photoinduced e^-. The corresponding reactions in the BiOBr/MoS_2/PMS/*hv* system are illustrated as follows:

Part I: $BiOBr/MoS_2+hv \rightarrow h^+ + e^-$

$e^- + O_2 \rightarrow O_2^{\bullet-}$

$e^- + HSO_5^- \rightarrow SO_4^{\bullet-} + OH^-$

$e^- + Cr^{6+} \rightarrow Cr^{3+}$

$Mo^{4+} + Cr^{6+} \rightarrow Mo^{5+} + Cr^{3+}$

Part II: $Mo^{4+} + HSO_5^- \rightarrow Mo^{5+} + SO_4^{\bullet-}$

$Mo^{5+} + HSO_5^- \rightarrow Mo^{6+} + SO_4^{\bullet-}$

$Mo^{4+} + HSO_5^- \rightarrow Mo^{5+} + SO_4^{2-} + \bullet OH$

$SO_4^{\bullet-} + H_2O \rightarrow SO_4^{-} + \bullet OH + H^+$

$O_2^{\bullet-}/SO_4^{\bullet-}/\bullet OH/h^+$ + organic pollutants → small molecules

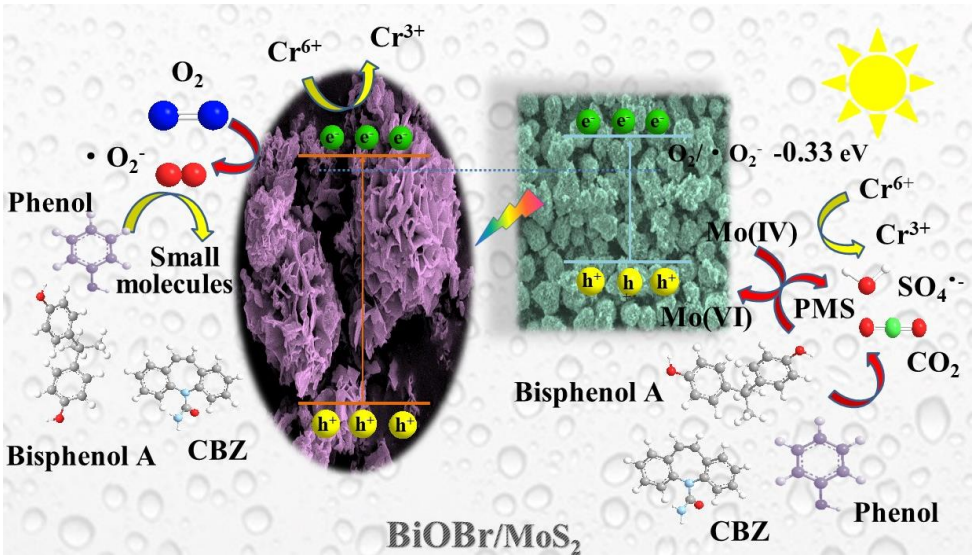

Fig.9 Proposed catalytic mechanism of various aromatic organic pollutants in the BiOBr-MoS_2/PMS/*hv* system

3.5 Practical applications of BiOBr/MoS_2 heterojunctions in PMS/hv systems

To explore the practical potential of BiOBr/MoS_2 heterojunctions, refractory pollutants phenol (an organic chemical raw material), bisphenol A (a phenolic endocrine disruptor) and carbamazepine (a tricyclic substance as psychiatric drug) were additionally studied in this work, which can effectively avoid the interference of catalyst sensitized by organic dyes [50]. As shown in Fig. S10, no degradation of phenol, bisphenol A and carbamazepine were detected in the absence of catalyst, illustrating that self-decomposition of these organic pollutants was negligible. Only with addition of BiOBr, MoS_2 and BiOBr/MoS_2 catalysts did the concentration of various pollutants gradually decrease. In comparison with pristine BiOBr and MoS_2, the catalytic efficiency via BiOBr/MoS_2 heterojunctions significantly improved, which achieved an ultimate degradation rate of about 62.1, 72.5 and 85.5 % for phenol, bisphenol A and carbamazepine, respectively. Moreover, the total organic

carbon removal efficiencies of phenol, bisphenol A and carbamazepine reached 43.6, 49.8 and 50.3%, indicating excellent oxidative capacity for refractory organic pollutants.

To investigate the degradation process, HPLC was used for detecting the concentration and decomposition pathways of phenol in treated solutions. As presented in Fig.10, the 2D chromatogram of HPLC over $BiOBr/MoS_2$ catalyst indicated that retention time (RT) of the phenol peak was about 2.6 min. As the irradiation time increased, the characteristic peak intensity gradually decreased and appeared to be steady after 90 min. During the phenol degradation process in the PMS/*hv* system, several new peaks at RT of 2.24, 1.83, 1.76, 1.50 min gradually appeared, indicating that phenol had been decomposed after 30 min, and that new intermediates were generated. Generally, phenol can be attacked by the photo-generated h^+ and reactive oxygen species such as $SO_4^{\cdot-}$, $\cdot OH$, and $\cdot O_2^-$, and transformed into *o*-diphenol, hydroquinone, benzoquinone and other compounds [39]. These molecules could be continually decomposed and converted into other substances, such as fumaric acid and malonic acid [51], which could be further mineralized into carbon dioxide and water (Fig.10 and Fig.S11, decomposition pathway). These superior degradation capacities for phenol, bisphenol A and carbamazepine measured by UV-vis spectroscopy and HPLC indicated the remarkable oxidative capacity of $BiOBr/MoS_2$ heterojunctions for phenolic and pharmaceutical pollutant decomposition.

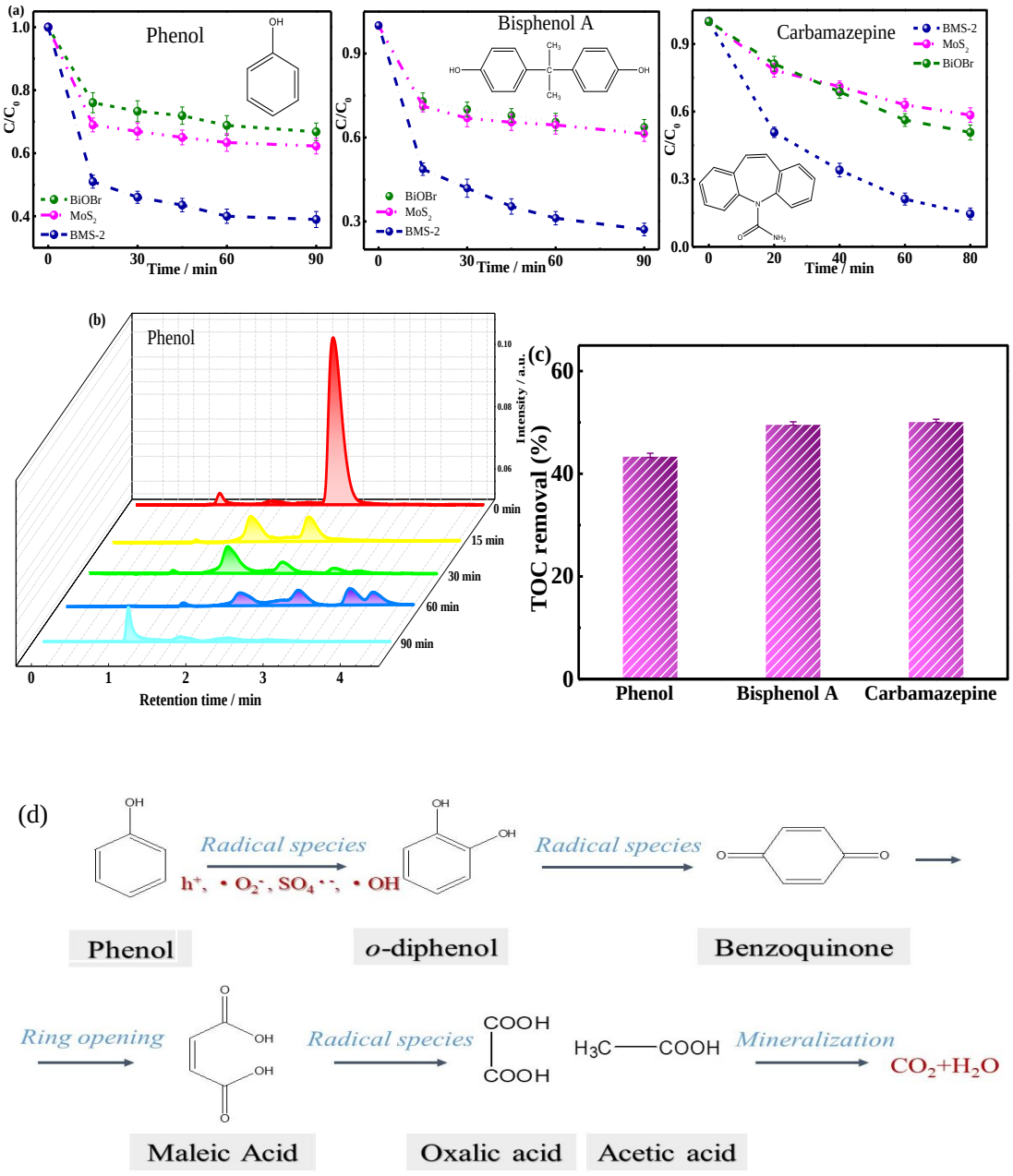

Fig. 10 (a) The degradation of phenol, bisphenol A and carbamazepine; (b) the HPLC chromatogram of phenol; (c) the TOC removal efficiency of phenol, bisphenol A and carbamazepine; (d) the degradation pathway of phenol by BMS-2 via PMS activation under visible light irradiation. Reaction conditions: catalyst=0.5 g/L, [PMS]=1 mM (photo-Fenton), pollutants=20 mg/L.

The stability of BMS-2 catalyst was investigated via five cyclic experiments by visible light assisted-PMS activation. As displayed in Fig.11a, RhB could be

599 completely degraded and the degradation efficiency still maintained a stable level
600 after five consecutive cycles. The slight decrease along the fifth recycling experiment
601 may contribute to low loss and the generated organic intermediates. Furthermore, the
602 chemical structure of sample BMS-2 was characterized by FTIR, XRD, XPS, SEM
603 and TEM before and after the photo-Fenton catalytic reaction. After using five times,
604 the XRD patterns (Fig.11b) and FTIR (Fig.11c) and XPS spectra (Fig.S12) did not
605 exhibit obvious modification and the original peaks were preserved very well.
606 Additionally, the hierarchical structure established by MoS_2 and BiOBr nanosheets
607 was not destroyed and the lattice distances were completely in accordance with those
608 for fresh samples (Fig. S12), underlining the robust prospect of BiOBr/MoS_2 for large
609 scale application and recovery.

610 To explore the industrial application potential of BiOBr/MoS_2 catalysts, a
611 scaled-up experiment from 10 mL to 3.0 L was conducted. As shown in Fig.11d, the
612 BMS-2 composite still exhibited stable catalytic activity for visible light-driven PMS
613 activation. After 30 min, the degradation efficiency of about 100% was achieved and
614 the kinetics were fitted as a first-order reaction (Fig.S13). The reaction rate constant *k*,
615 for the BMS-2 was 5.31 and 4.53 times that of the pristine MoS_2 and BiOBr catalysts.
616 The mineralization conversion rates (TOC) were measured in a 3.0 L solution
617 (Fig.11e) and it was found that efficiency achieved 50.05% during 30 min of
618 illumination, implying the excellent mineralization ability of BMS-2 photo-Fenton
619 catalyst. Notably, the mineralization rate was lower than the decomposition rate
620 (99.9%), which is mainly ascribed to the generated organic intermediates during the

decomposition process [52]. Moreover, the catalytic capacity of BiOBr/MoS_2 is also applicable for various pollutants in the presence of PMS under the 3L scaled-up experiment, such as phenol, bisphenol A and carbamazepine (Fig.11f), further highlighting the potential for industrial advanced oxidation processes.

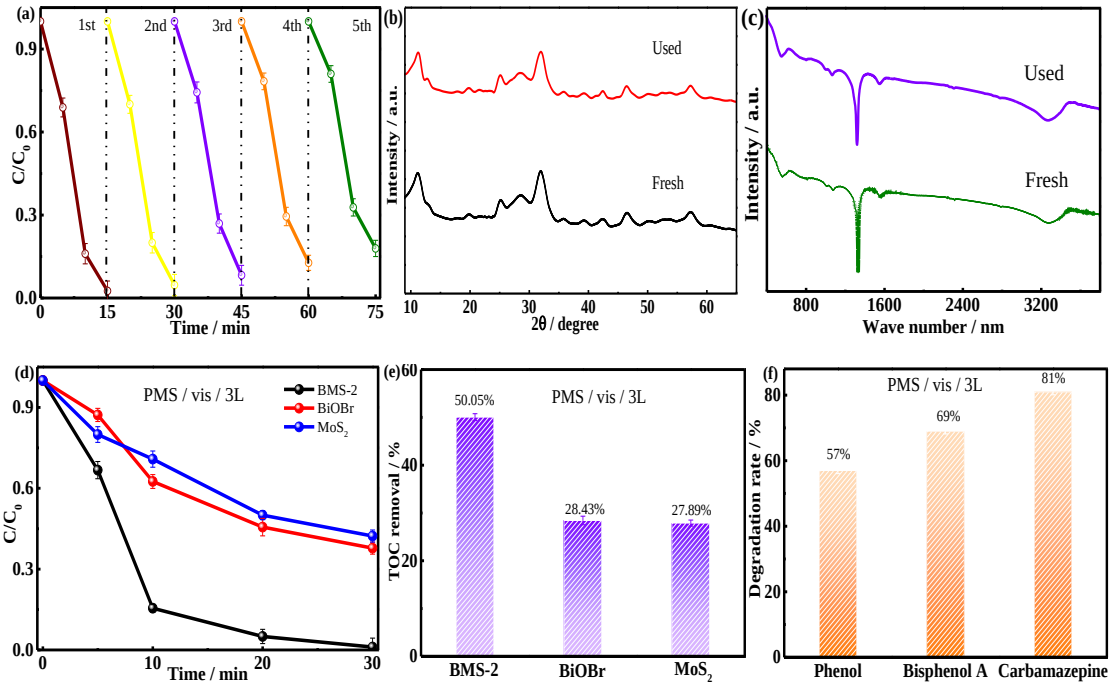

Fig.11 (a) Stability test of the catalytic activity using BMS-2 in the PMS/*hv* system, (b) XRD pattern, (c) FTIR spectrum of BMS-2 before and after five cycles; (d) Visible light-driven PMS activation for the degradation of RhB in a 3.0-L solution, (e) TOC mineralization efficiency of RhB by BiOBr, MoS_2 and BMS-2, (f) Degradation rate of phenol, bisphenol A and carbamazepine in a 3.0-L solution in BiOBr-MoS_2/PMS/*hv* system. Reaction conditions: catalyst=0.5 g/L, [PMS]=1 mM (photo-Fenton), pollutants=20 mg/L.

4. Conclusions

In this work, 2D/2D BiOBr/MoS_2 heterojunctions are reported as extraordinary catalysts for PMS activation in photo-Fenton systems. Characterization indicated that MoS_2 nanolayers were stably integrated on the surface of flower-like hierarchical

BiOBr nanosheets, exhibiting rapid charge carrier separation and migration via the closely bonded Type-II heterojunction structure. During the BiOBr/MoS_2/PMS/*hv* system, the heterojunction exhibited promoted catalytic capacity for various refractory organic contaminants compared with BiOBr, MoS_2 and previous reports [53, 54]. The superior mineralization efficiency and possible degradation pathways of phenol were further validated. As an electron acceptor, PMS can be effectively activated via photoinduced electrons and exposed Mo sites with multivalence and multiphase in composites, resulting in a swift separation of h^+-e^- pairs, prolonged lifetime of electrons and higher oxidative ability of holes compared with photo-systems. Trapping experiments and EPR analysis demonstrated that $SO_4^{\cdot-}$, ·OH, $\cdot O_2^-$ and h^+ simultaneously played major roles in pollutant degradation under visible light assisted-PMS activation systems. Impressively, this work not only provides an outstanding catalyst with high stability and excellent scale-up performance, but also opens a new perspective on PMS activation mechanism. Further study can be conducted at a larger pilot-scale for practical complexed flowing real wastewater treatment.

Acknowledgements

This work was supported by the Tokyo Human Resources Fund for City Diplomacy (H29-1).

Reference:

[1] S. Zhan, H. Zhang, X. Mi, Y. Zhao, C. Hu, L. Lyu, Efficient Fenton-like Process for Pollutant Removal in Electron-Rich/Poor Reaction Sites Induced by Surface Oxygen Vacancy over Cobalt–Zinc Oxides, Environmental Science & Technology, 54 (2020) 8333-8343.

[2] Y. Zhou, L. Zhou, Y. Zhou, M. Xing, J. Zhang, Z-scheme photo-Fenton system for efficiency synchronous oxidation of organic contaminants and reduction of metal ions, Applied Catalysis B: Environmental, 279 (2020) 119365.

[3] Y. Gao, Y. Zhu, L. Lyu, Q. Zeng, X. Xing, C. Hu, Electronic Structure Modulation of Graphitic Carbon Nitride by Oxygen Doping for Enhanced Catalytic Degradation of Organic Pollutants through Peroxymonosulfate Activation, Environ Sci Technol, 52 (2018) 14371-14380.

[4] Y. Gao, Y. Zhu, Z. Chen, C. Hu, Nitrogen-Coordinated Cobalt Embedded in a Hollow Carbon Polyhedron for Superior Catalytic Oxidation of Organic Contaminants with Peroxymonosulfate, ACS ES&T Engineering, (2020).

[5] X. Luo, L. Bai, J. Xing, X. Zhu, D. Xu, B. Xie, Z. Gan, G. Li, H. Liang, Ordered Mesoporous Cobalt Containing Perovskite as a High-Performance Heterogeneous Catalyst in Activation of Peroxymonosulfate, ACS Appl Mater Interfaces, 11 (2019) 35720-35728.

[6] T. Chen, Z. Zhu, H. Zhang, Y. Qiu, D. Yin, G. Zhao, Facile Construction of a Copper-Containing Covalent Bond for Peroxymonosulfate Activation: Efficient Redox Behavior of Copper Species via Electron Transfer Regulation, ACS Appl

682 Mater Interfaces, 12 (2020) 42790-42802.
683 [7] F. Chen, G.X. Huang, F.B. Yao, Q. Yang, Y.M. Zheng, Q.B. Zhao, H.Q. Yu,
684 Catalytic degradation of ciprofloxacin by a visible-light-assisted peroxymonosulfate
685 activation system: Performance and mechanism, Water Res, 173 (2020) 115559.
686 [8] T. Taniguchi, L. Nurdiwijayanto, S. Li, H.E. Lim, Y. Miyata, X. Lu, R. Ma, D.-M.
687 Tang, S. Ueda, K. Tsukagoshi, T. Sasaki, M. Osada, On/Off Boundary of
688 Photocatalytic Activity between Single- and Bilayer MoS2, ACS Nano, 14 (2020)
689 6663-6672.
690 [9] M. Dan, J. Xiang, F. Wu, S. Yu, Q. Cai, L. Ye, Y. Ye, Y. Zhou, Rich
691 active-edge-site MoS_2 anchored on reduction sites in metal sulfide heterostructure:
692 Toward robust visible light photocatalytic hydrogen sulphide splitting, Applied
693 Catalysis B: Environmental, 256 (2019) 117870.
694 [10] Y. Yang, Y. Wang, H.-L. He, W. Yan, L. Fang, Y.-B. Zhang, Y. Qin, R. Long,
695 X.-M. Zhang, X. Fan, Covalently Connected $Nb_4N_{5-x}O_x$–MoS_2 Heterocatalysts with
696 Desired Electron Density to Boost Hydrogen Evolution, ACS Nano, 14 (2020)
697 4925-4937.
698 [11] J. Jian, Y. Li, H. Bi, X. Wang, X. Wu, W. Qin, Aluminum Decoration on MoS_2
699 Ultrathin Nanosheets for Highly Efficient Hydrogen Evolution, ACS Sustainable
700 Chemistry & Engineering, 8 (2020) 4547-4554.
701 [12] X. Xin, Y. Song, S. Guo, Y. Zhang, B. Wang, J. Yu, X. Li, In-situ growth of
702 high-content 1T phase MoS_2 confined in the CuS nanoframe for efficient
703 photocatalytic hydrogen evolution, Applied Catalysis B: Environmental, 269 (2020)

118773.

[13] M. Xing, W. Xu, C. Dong, Y. Bai, J. Zeng, Y. Zhou, J. Zhang, Y. Yin, Metal Sulfides as Excellent Co-catalysts for H_2O_2 Decomposition in Advanced Oxidation Processes, Chem, 4 (2018) 1359-1372.

[14] H. Zhou, L. Lai, Y. Wan, Y. He, G. Yao, B. Lai, Molybdenum disulfide (MoS_2): A versatile activator of both peroxymonosulfate and persulfate for the degradation of carbamazepine, Chemical Engineering Journal, 384 (2020).

[15] Y. Chen, G. Zhang, Q. Ji, H. Liu, J. Qu, Triggering of Low-Valence Molybdenum in Multiphasic MoS_2 for Effective Reactive Oxygen Species Output in Catalytic Fenton-like Reactions, ACS Appl Mater Interfaces, 11 (2019) 26781-26788.

[16] Q.-Y. Tang, M.-J. Yang, S.-Y. Yang, Y.-H. Xu, Enhanced photocatalytic degradation of glyphosate over 2D CoS/BiOBr heterojunctions under visible light irradiation, Journal of Hazardous Materials, 407 (2021) 124798.

[17] Z. Wang, L. Jiang, K. Wang, Y. Li, G. Zhang, Novel AgI/$BiSbO_4$ heterojunction for efficient photocatalytic degradation of organic pollutants under visible light: Interfacial electron transfer pathway, DFT calculation and degradation mechanism study, Journal of Hazardous Materials, (2020) 124948.

[18] Y. Fu, Z. Ren, J. Wu, Y. Li, W. Liu, P. Li, L. Xing, J. Ma, H. Wang, X. Xue, Direct Z-scheme heterojunction of ZnO/MoS_2 nanoarrays realized by flowing-induced piezoelectric field for enhanced sunlight photocatalytic performances, Applied Catalysis B: Environmental, 285 (2021) 119785.

[19] M. Dan, S. Wei, D.E. Doronkin, Y. Li, Z. Zhao, S. Yu, J.-D. Grunwaldt, Y. Lin, Y.

Zhou, Novel MnS/(In_xCu_{1-x})$_2S_3$ composite for robust solar hydrogen sulphide splitting via the synergy of solid solution and heterojunction, Applied Catalysis B: Environmental, 243 (2019) 790-800.

[20] Y. Liu, Z. Hu, J.C. Yu, Fe Enhanced Visible-Light-Driven Nitrogen Fixation on BiOBr Nanosheets, Chemistry of Materials, 32 (2020) 1488-1494.

[21] P. Li, Z. Zhou, Q. Wang, M. Guo, S. Chen, J. Low, R. Long, W. Liu, P. Ding, Y. Wu, Y. Xiong, Visible-Light-Driven Nitrogen Fixation Catalyzed by Bi_5O_7Br Nanostructures: Enhanced Performance by Oxygen Vacancies, Journal of the American Chemical Society, 142 (2020) 12430-12439.

[22] X. Wu, N. Liu, M. Wang, Y. Qiu, B. Guan, D. Tian, Z. Guo, L. Fan, N. Zhang, A Class of Catalysts of BiOX (X = Cl, Br, I) for Anchoring Polysulfides and Accelerating Redox Reaction in Lithium Sulfur Batteries, ACS Nano, 13 (2019) 13109-13115.

[23] D. Majhi, K. Das, A. Mishra, R. Dhiman, B.G. Mishra, One pot synthesis of CdS/BiOBr/$Bi_2O_2CO_3$: A novel ternary double Z-scheme heterostructure photocatalyst for efficient degradation of atrazine, Applied Catalysis B: Environmental, 260 (2020) 118222.

[24] S.J. Clark, M.D. Segall, C.J. Pickard, P.J. Hasnip, M.I.J. Probert, K. Refson, M.C. Payne, First principles methods using CASTEP, Zeitschrift für Kristallographie - Crystalline Materials, 220 (2005) 567-570.

[25] J.P. Perdew, K. Burke, M. Ernzerhof, Generalized gradient approximation made simple, Physical Review Letters, 77 (1996) 3865-3868.

748 [26] B. Zhang, M. Zhang, L. Zhang, P.A. Bingham, W. Li, S. Kubuki, PVP
749 surfactant-modified flower-like BiOBr with tunable bandgap structure for efficient
750 photocatalytic decontamination of pollutants, Applied Surface Science, 530 (2020)
751 147233.
752 [27] S. Zhang, S. Duan, G. Chen, S. Meng, X. Zheng, Y. Fan, X. Fu, S. Chen,
753 $MoS_2/Zn_3In_2S_6$ composite photocatalysts for enhancement of visible light-driven
754 hydrogen production from formic acid, Chinese Journal of Catalysis, 42 (2021)
755 193-204.
756 [28] H. Li, T. Hu, N. Du, R. Zhang, J. Liu, W. Hou, Wavelength-dependent
757 differences in photocatalytic performance between BiOBr nanosheets with dominant
758 exposed (001) and (010) facets, Applied Catalysis B: Environmental, 187 (2016)
759 342-349.
760 [29] F. Guo, X. Huang, Z. Chen, H. Ren, M. Li, L. Chen, MoS_2 nanosheets anchored
761 on porous $ZnSnO_3$ cubes as an efficient visible-light-driven composite photocatalyst
762 for the degradation of tetracycline and mechanism insight, Journal of Hazardous
763 Materials, 390 (2020) 122158.
764 [30] Y. Geng, D. Chen, N. Li, Q. Xu, H. Li, J. He, J. Lu, Z-Scheme 2D/2D
765 α-Fe_2O_3/g-C_3N_4 heterojunction for photocatalytic oxidation of nitric oxide, Applied
766 Catalysis B: Environmental, 280 (2021) 119409.
767 [31] H. Tian, S. Zhu, F. Xu, W. Mao, H. Wei, Y. Mai, X. Feng, Growth of 2D
768 Mesoporous Polyaniline with Controlled Pore Structures on Ultrathin MoS_2
769 Nanosheets by Block Copolymer Self-Assembly in Solution, ACS Applied Materials

770 & Interfaces, 9 (2017) 43975-43982.
771 [32] M. Dan, Q. Zhang, S. Yu, A. Prakash, Y. Lin, Y. Zhou, Noble-metal-free
772 MnS/In_2S_3 composite as highly efficient visible light driven photocatalyst for H_2
773 production from H_2S, Applied Catalysis B: Environmental, 217 (2017) 530-539.
774 [33] S. Cao, Y. Zhang, N. He, J. Wang, H. Chen, F. Jiang, Metal-free 2D/2D
775 heterojunction of covalent triazine-based frameworks/graphitic carbon nitride with
776 enhanced interfacial charge separation for highly efficient photocatalytic elimination
777 of antibiotic pollutants, J Hazard Mater, 391 (2020) 122204.
778 [34] T. Zhang, Y. Chen, T. Leiknes, Oxidation of Refractory Benzothiazoles with
779 $PMS/CuFe_2O_4$: Kinetics and Transformation Intermediates, Environmental Science &
780 Technology, 50 (2016) 5864-5873.
781 [35] L. Zhu, J. Ji, J. Liu, S. Mine, M. Matsuoka, J. Zhang, M. Xing, Designing
782 3D-MoS_2 Sponge as Excellent Cocatalysts in Advanced Oxidation Processes for
783 Pollutant Control, Angew Chem Int Ed Engl, 59 (2020) 13968-13976.
784 [36] S. Li, J. Chen, S. Hu, H. Wang, W. Jiang, X. Chen, Facile construction of novel
785 Bi_2WO_6/Ta_3N_5 Z-scheme heterojunction nanofibers for efficient degradation of
786 harmful pharmaceutical pollutants, Chemical Engineering Journal, 402 (2020).
787 [37] Q. Jiang, Y. Zhang, S. Jiang, Y. Wang, H. Li, W. Han, J. Qu, L. Wang, Y. Hu,
788 Graphene-like carbon sheet-supported nZVI for efficient atrazine oxidation
789 degradation by persulfate activation, Chemical Engineering Journal, 403 (2021).
790 [38] S. Qu, W. Wang, X. Pan, C. Li, Improving the Fenton catalytic performance of
791 FeOCl using an electron mediator, J Hazard Mater, 384 (2020) 121494.

792 [39] Z. Mo, K. Wang, H. Yang, Z. Ou, Y. Tong, T. Yu, Y. Wang, P. Tsiakaras, S. Song,
793 Heterojunction architecture of pTTh nanoflowers with CuO_x nanoparticles hybridized
794 for efficient photoelectrocatalytic degradation of organic pollutants, Applied Catalysis
795 B: Environmental, 277 (2020).
796 [40] Q. Yi, J. Ji, B. Shen, C. Dong, J. Liu, J. Zhang, M. Xing, Singlet Oxygen
797 Triggered by Superoxide Radicals in a Molybdenum Cocatalytic Fenton Reaction
798 with Enhanced REDOX Activity in the Environment, Environ Sci Technol, 53 (2019)
799 9725-9733.
800 [41] Y. Zhou, L. Zhou, Y. Zhou, M. Xing, J. Zhang, Z-scheme photo-Fenton system
801 for efficiency synchronous oxidation of organic contaminants and reduction of metal
802 ions, Applied Catalysis B: Environmental, 279 (2020).
803 [42] S. Wang, B. Zhu, M. Liu, L. Zhang, J. Yu, M. Zhou, Direct Z-scheme ZnO/CdS
804 hierarchical photocatalyst for enhanced photocatalytic H_2-production activity, Applied
805 Catalysis B: Environmental, 243 (2019) 19-26.
806 [43] V.L. Chevrier, S.P. Ong, R. Armiento, M.K.Y. Chan, G. Ceder, Hybrid density
807 functional calculations of redox potentials and formation energies of transition metal
808 compounds, Physical Review B, 82 (2010).
809 [44] J. Ali, L. Wenli, A. Shahzad, J. Ifthikar, G.G. Aregay, Shahib, II, Z. Elkhlifi, Z.
810 Chen, Z. Chen, Regulating the redox centers of Fe through the enrichment of Mo
811 moiety for persulfate activation: A new strategy to achieve maximum persulfate
812 utilization efficiency, Water Res, 181 (2020) 115862.
813 [45] L. Wang, D. Yan, L. Lyu, C. Hu, N. Jiang, L. Zhang, Notable light-free catalytic

activity for pollutant destruction over flower-like BiOI microspheres by a dual-reaction-center Fenton-like process, J Colloid Interface Sci, 527 (2018) 251-259.

[46] J. Jiang, X. Wang, Y. Liu, Y. Ma, T. Li, Y. Lin, T. Xie, S. Dong, Photo-Fenton degradation of emerging pollutants over Fe-POM nanoparticle/porous and ultrathin g-C_3N_4 nanosheet with rich nitrogen defect: Degradation mechanism, pathways, and products toxicity assessment, Applied Catalysis B: Environmental, 278 (2020).

[47] Z. Wang, C. Lai, L. Qin, Y. Fu, J. He, D. Huang, B. Li, M. Zhang, S. Liu, L. Li, W. Zhang, H. Yi, X. Liu, X. Zhou, ZIF-8-modified $MnFe_2O_4$ with high crystallinity and superior photo-Fenton catalytic activity by Zn-O-Fe structure for TC degradation, Chemical Engineering Journal, 392 (2020).

[48] F. Chen, Q. Yang, F. Yao, Y. Ma, Y. Wang, X. Li, D. Wang, L. Wang, H. Yu, Synergetic transformations of multiple pollutants driven by $BiVO_4$-catalyzed sulfite under visible light irradiation: Reaction kinetics and intrinsic mechanism, Chemical Engineering Journal, 355 (2019) 624-636.

[49] Z. Li, R. Fan, Z. Hu, W. Li, H. Zhou, S. Kang, Y. Zhang, H. Zhang, G. Wang, Ethanol introduced synthesis of ultrastable 1T-MoS_2 for removal of Cr(VI), J Hazard Mater, 394 (2020) 122525.

[50] L. Gui, Z. Chen, B. Chen, Y. Song, Q. Yu, W. Zhu, Q. Hu, Y. Liu, Z. Zheng, L. Ze, H. You, F. Yeasmin, Preparation and characterization of ZnO/PEG-Co(II)-PbO_2 nanocomposite electrode and an investigation of the electrocatalytic degradation of phenol, J Hazard Mater, 399 (2020) 123018.

[51] J. Gao, Y. Liu, X. Xia, L. Wang, W. Dong, Fe1-xZnxS ternary solid solution as an

836 efficient Fenton-like catalyst for ultrafast degradation of phenol, J Hazard Mater, 353
837 (2018) 393-400.
838 [52] J. Ni, W. Wang, D. Liu, Q. Zhu, J. Jia, J. Tian, Z. Li, X. Wang, Z. Xing, Oxygen
839 vacancy-mediated sandwich-structural TiO_{2-x} /ultrathin g-C_3N_4/TiO_{2-x} direct
840 Z-scheme heterojunction visible-light-driven photocatalyst for efficient removal of
841 high toxic tetracycline antibiotics, J Hazard Mater, (2020) 124432.
842 [53] T. Chankhanittha, S. Nanan, Visible-light-driven photocatalytic degradation of
843 ofloxacin (OFL) antibiotic and Rhodamine B (RhB) dye by solvothermally grown
844 ZnO/Bi_2MoO_6 heterojunction, Journal of Colloid and Interface Science, 582 (2021)
845 412-427.
846 [54] C. Chen, M. Li, Y. Jia, R. Chong, L. Xu, X. Liu, Surface defect-engineered silver
847 silicate/ceria p-n heterojunctions with a flower-like structure for boosting visible light
848 photocatalysis with mechanistic insight, Journal of Colloid and Interface Science, 564
849 (2020) 442-453.
850